AIAA AVIATION Forum
8-12 June 2026, San Diego, CA
AIAA AVIATION 2026 Forum

10.2514/6.2026-4363



# Linear and Numerical Analysis of Interfacial Instabilities in Vibrated Cylindrical Containers

Tianyi Chu* and Benjamin Wilfong.†
*School of Computational Science & Engineering, Georgia Institute of Technology, Atlanta, Georgia 30332, USA*

Timothy Koehler‡ and Ryan M. McMullen§
*Engineering Sciences Center, Sandia National Laboratories, Albuquerque, New Mexico 87185, USA*

Spencer H. Bryngelson¶
*School of Computational Science & Engineering, Georgia Institute of Technology, Atlanta, Georgia 30332, USA*
*Daniel Guggenheim School of Aerospace Engineering, Georgia Institute of Technology, Atlanta, Georgia 30332, USA*
*George W. Woodruff School of Mechanical Engineering, Georgia Institute of Technology, Atlanta, Georgia 30332, USA*



**Fluid–fluid interfacial instabilities and the resulting mixing processes are ubiquitous in engineering applications, particularly within cylindrical containers due to their widespread use. In vertically vibrated, density-contrast configurations, the interface can destabilize through two fundamental hydrodynamic instabilities: the pressure-gradient-driven Rayleigh–Taylor (RT) instability and the parametric, resonance-induced Faraday instability. While each mechanism has been extensively studied in isolation, their coupled behavior in cylindrical coordinates remains poorly understood. Here, we investigate the interplay between the RT and Faraday instabilities in cylindrical geometry using linear Floquet stability analysis together with three-dimensional direct numerical simulations (DNS). Owing to the cylindrical confinement, the dominant spatial structures are naturally organized into Bessel eigenmodes at each azimuthal wavenumber: RT dynamics manifest as long-wavelength modes that grow monotonically, whereas Faraday responses excite shorter-wavelength modes with harmonic (H) or subharmonic (SH) Floquet time dependence. We analyze the instability mechanisms and spatiotemporal behavior across the oscillation frequency–amplitude parameter space, resolved by azimuthal wavenumber, Floquet harmonic, and radial mode index. The results show how vibration and density contrast jointly govern mode selection and interfacial evolution in confined cylindrical systems.**

## I. Nomenclature

| | | |
|---|---|---|
| $a$ | = | amplitude of oscillation |
| $\alpha$ | = | volume fraction |
| At | = | Atwood number |
| Bd | = | Bond number |
| $C$ | = | Viscous-to-gravitational force ratio |
| d$t$ | = | time step |
| $e$ | = | internal energy |
| $g$ | = | gravitational acceleration |
| $\gamma$ | = | Floquet exponent |

*Postdoctoral Fellow, School of Computational Science & Engineering, Member AIAA.
†Graduate student. School of Computational Science & Engineering.
‡Principal Member of the Technical Staff, Engineering Sciences Center.
§Senior Member of the Technical Staff, Engineering Sciences Center.
¶Assistant Professor, School of Computational Science and Engineering, Daniel Guggenheim School of Aerospace Engineering, George W. Woodruff School of Mechanical Engineering, Member AIAA.

$H$ = thickness of each fluid layer
$i$ = Bessel mode index
$j$ = phase of fluid
$m$ = azimuthal wavenumber
$n$ = harmonic index
$\mu$ = viscosity
$\omega$ = oscillatory frequency
$\mathbf{\Omega}$ = capillary stress tensor
$p$ = pressure
$r$ = radial coordinate
$R$ = cylinder radius
$\rho$ = density
$\sigma$ = surface tension
$t$ = time
$\boldsymbol{T}$ = viscous stress tensor
$\theta$ = azimuthal angle
$\boldsymbol{u}$ = velocity vector
$u_r$, $u_\theta$ = radial and azimuthal velocity components
$w$ = vertical velocity component
$\xi$ = cylinder aspect ratio
$Y$ = mass fraction
$z$ = vertical coordinate
$\zeta$ = interface displacement

Super- and subscripts

$(\cdot)'$ = fluctuating component
$\widehat{(\cdot)}$ = Fourier component
$(\cdot)^{(d)}$, $(\cdot)^{(l)}$ = denser and lighter fluids
$(\cdot)_{m,n,i}$ = Triplet of azimuthal wavenumber, Floquet harmonic index, and Bessel mode index

## II. Introduction

The interface separating phases in multiphase fluid systems is often susceptible to deformation driven by internal density differences or external vibrations. Unstable growth of these interfacial perturbations can ultimately result in interface breakup and fluid mixing. In engineering applications, these phenomena frequently occur within cylindrical containers due to their widespread use in systems such as fuel tanks, atomization devices, and inertial confinement fusion setups [1, 2]. Therefore, understanding the underlying instability mechanisms in cylindrical coordinates is fundamental to predict and control interfacial dynamics in these systems accurately.

Without restricting the system to a specific coordinate system, linear stability analysis identifies two primary hydrodynamic instability mechanisms: the pressure-gradient-driven mechanism, which gives rise to Rayleigh–Taylor (RT) instability [3, 4], and the parametric resonance mechanism, which leads to Faraday instability [5]. Decades of research have focused on investigating these fundamental hydrodynamic instabilities in confined cylindrical containers. Wolf [6, 7] experimentally demonstrated that viscous RT instabilities can be dynamically stabilized *without* inducing standing Faraday waves, by oscillating the container at specific amplitudes and frequencies. This form of stabilization in cylindrical geometries has also been theoretically examined in the thin liquid film limit [8, 9]. More recently, Liang and Luo [10] experimentally studied a water–air interface and showed cylindrical RT instabilities that depend on the azimuthal wavenumber. In parallel, extensive theoretical and experimental efforts have also been devoted to Faraday-type surface waves in cylinders,

both for free [11, 12] and pinned contact lines [13–15]. Linear stability predictions have also been validated through measurements of the Faraday threshold in cylinders at low forcing frequencies [16], and against observed pattern formation in forced cylindrical configurations [17].

Despite their well-established nature and widespread observation, a comprehensive understanding of the interaction between RT and Faraday instabilities within cylindrical containers remains lacking. Such understanding is critical for a wide range of engineering applications, including industrial mixing processes and multiphase fluids in spacecraft propellant tanks, where external vibrations and internal density contrasts often coexist. To this end, the present study builds upon our recent analysis in a two-dimensional infinite domain [18], extending it to three-dimensional (3D) confined cylindrical coordinates. Using linear Floquet stability theory and direct numerical simulations (DNS), we investigate the temporal and spatial dynamics of both long-wavelength-like RT and short-wavelength-like Faraday structures.

The remainder of the paper is organized as follows. In section III, we performed a linear Floquet stability analysis to characterize the temporal evolution of interfacial and flow-field modes for each azimuthal wavenumber. Section IV describes the numerical method for three-dimensional, scale-resolved DNS of the two-phase fluid system. In section V, these simulations are used to validate the linear predictions and to examine the subsequent evolution into multiscale and nonlinear regimes, where complex interfacial patterns emerge. Lastly, Section VI summarizes the main findings and discusses the coexistence and competition of RT and Faraday instabilities in cylindrical containers.



## III. Theoretical Background

### A. Governing equations

Consider the interface between two immiscible and incompressible fluids: a denser and lighter fluid, denoted by subscripts $(\cdot)^{(d)}$ and $(\cdot)^{(l)}$. The two fluids are contained within a cylindrical vessel with a height of $2H$ and a radius of $R$, with the interface located at the mid-height $H$. The container is subject to constant gravitational acceleration and an oscillatory vertical acceleration

$$\tilde{g}(t) = g_{\text{sgn}} g + a\cos(\omega t + \varphi_0), \tag{1}$$

where $a$ is the oscillatory amplitude, $\omega$ is the corresponding frequency, and $\varphi_0$ is the initial phase. Positive gravity, $g_{\text{sgn}} = 1$, applies when the denser fluid is at the bottom domain, and negative gravity, $g_{\text{sgn}} = -1$, applies when the denser fluid is on top. Within each fluid layer $j$, the motion of the fluid is governed by the incompressible Navier–Stokes equations,

$$\rho^{(j)}\left[\partial_t + \left(\boldsymbol{u}^{(j)}\cdot\boldsymbol{\nabla}\right)\right]\boldsymbol{u}^{(j)} = -\boldsymbol{\nabla}p^{(j)} - \rho^{(j)}\tilde{g}\boldsymbol{e}_z + \mu^{(j)}\boldsymbol{\nabla}^2\boldsymbol{u}^{(j)}, \quad \nabla\cdot\boldsymbol{u}^{(j)} = 0. \tag{2}$$

To systematically analyze the interfacial dynamics, we nondimensionalize the governing equations using $H$ as the characteristic length and $g$ as the reference gravitational acceleration. The gravitational time is defined as $t_c = \sqrt{H/g}$. Density, $\rho$, viscosity, $\mu$, and surface tension, $\sigma$, are scaled using appropriate reference values. The resulting dimensionless variables, denoted by $(\cdot)^*$, are summarized in table 1.

The dimensionless version of equation (2) is

$$\left[\partial_{t^*} + \left(\boldsymbol{u}^{*(j)}\cdot\boldsymbol{\nabla}^*\right)\right]\boldsymbol{u}^{*(j)} = -\boldsymbol{\nabla}^* p^{*(j)} - \tilde{g}^*\boldsymbol{e}_z + C^{(j)}\boldsymbol{\Delta}^*\boldsymbol{u}^{*(j)}, \quad \boldsymbol{\nabla}^*\cdot\boldsymbol{u}^{*(j)} = 0, \tag{3}$$

where $C^{(d)} = C$, and $C^{(l)} = (1-\text{At})/(\eta(1+\text{At}))$. We can decompose the flow state around the equilibrium-state solution of the Navier–Stokes equations (3) as

$$\boldsymbol{u}^{*(j)} = \boldsymbol{U}^{*(j)} + \boldsymbol{u}'^{*(j)}, \quad p^{*(j)} = P^{*(j)} + p'^{*(j)}, \tag{4}$$

where $(\boldsymbol{U}^{*(j)},\ P^{*(j)}) = (0, -\tilde{g}^*\boldsymbol{e}_z)$ and $(\cdot)'$ denotes the small fluctuating components. The linearized governing equations

**Table 1 Dimensionless quantities.**

| Dimensionless quantity | Quantity name |
|---|---|
| $\xi = H/R$ | Cylinder aspect ratio |
| $\mathrm{At} = (\rho^{(d)} - \rho^{(l)})/(\rho^{(d)} + \rho^{(l)})$ | Atwood number |
| $\eta = \mu^{(l)}/\mu^{(d)}$ | Viscosity ratio |
| $C = \nu^{(d)}/\sqrt{gH^3}$ | Viscous-to-gravitational force ratio |
| $\mathrm{Bd} = \rho^{(d)} g h^2/\sigma^{(d)}$ | Bond number |
| $a^* = a/g$ | Acceleration |
| $\zeta^* = \zeta/H$ | Interface displacement |
| $t^* = t/t_c$ | Time |
| $\gamma^* = \gamma t_c$ | Growth rate |
| $\omega^* = \omega t_c$ | Oscillatory frequency |
| $[u_r, u_\theta, w]^* = [u_r, u_\theta, w] t_c/H$ | Velocity components |

for the fluctuations are

$$\partial_{t^*} \boldsymbol{u'}^{*(j)} = -\boldsymbol{\nabla}^* p'^{*(j)} + C^{(j)} \boldsymbol{\Delta}^* \boldsymbol{u'}^{*(j)}, \quad \boldsymbol{\nabla}^* \cdot \boldsymbol{u'}^{*(j)} = 0. \tag{5}$$

Applying the operator $\boldsymbol{e}_z \cdot \boldsymbol{\nabla}^* \times \boldsymbol{\nabla}^* \times$ to equation (5) eliminates the horizontal velocity components, yielding

$$\left(\partial_{t^*} - C^{(j)} \boldsymbol{\Delta}^*\right) \boldsymbol{\Delta}^* w'^{*(j)} = 0, \tag{6}$$

At the interface $z^* = \zeta^*$, continuity of the vertical velocity perturbation, $w'^{*(j)}$, and the tangential stress yields

$$\delta \left[ w'^{*(j)},\ \partial_{z^*} \left( w'^{*(j)} \right),\ C^{(j)} \left( \boldsymbol{\Delta}^* - 2\partial_{z^* z^*} \right) w'^{*(j)} \right] = 0, \tag{7}$$

where $\delta$ represents the jump across the interface. The linearized kinematic boundary condition gives

$$\partial_{t^*} \zeta^* = w^*|_{z^*=0}. \tag{8}$$

The jump condition for pressure across the interface,

$$\delta p^* = 2(C^{(l)} - C^{(d)}) \left(\partial_{z^*} w^*\right)|_{z^*=0} - \frac{2\mathrm{At}}{1+\mathrm{At}} \tilde{g}^* \zeta^* + \frac{1}{\mathrm{Bd}} \left(\boldsymbol{\Delta}^* - \partial_{z^* z^*}\right) \zeta^*, \tag{9}$$

explicitly represents the effect of vibration. Together, equations (6) to (9) govern the linearized interfacial dynamics. We focus our analysis on the regime in which the interface profile, $\zeta^*$, remains well-defined and single-valued. At later times, as nonlinear effects become meaningful, the interface may evolve into a complex profile and can undergo breakup. For clarity, the superscript $(\cdot)^*$ denoting dimensionless variables is omitted henceforth. All variables are nondimensional unless otherwise specified.

### B. Linear Floquet stability analysis in cylindrical coordinates

Due to the rotational symmetry of the problem, a Fourier decomposition in the azimuthal direction is used to expand both the velocity field and the interface displacement. Given that the instability is hypothesized to be mainly driven by the time-periodic variation in gravity, a Floquet analysis is used to model the system's dynamics [19]. Specifically, the vertical displacement of the interface at each azimuthal wavenumber is expected to exhibit exponential growth or decay along with superimposed oscillatory fluctuations. The combined spatiotemporal decomposition for the vertical velocity

perturbation and the interface displacement is thus expressed as

$$\left[w'^{(j)}(\boldsymbol{x},z,t),\ \zeta(\boldsymbol{x},t)\right]=\sum_{m=-\infty}^{\infty}\underbrace{\left(\sum_{n=-\infty}^{\infty}\left[\hat{w}_{m,n}^{(j)}(r,z),\ \hat{\zeta}_{m,n}(r)\right]\mathrm{e}^{\mathrm{i}n\omega(t+t_0)}\right)}_{\text{Periodic component}}\underbrace{\mathrm{e}^{\gamma_m t}}_{\text{Modal}}\ \underbrace{\mathrm{e}^{\mathrm{i}m\theta}}_{\text{Azimuthal}},\tag{10}$$

where $\gamma_m$ is the Floquet exponent for the $m$th azimuthal wavenumber, $t_0$ is the time shift associated with the initial phase $\varphi_0$, and $n$ is the integer index of the harmonics [20, 21]. A positive real part of the Floquet exponent indicates instability, leading to the growth of perturbations and eventual interfacial breakup. Equation (10) decomposes the waveforms into different azimuthal wavenumbers and oscillation harmonics. Substituting this decomposition into the governing equation (6) yields

$$\mathcal{L}_{m,n}\hat{w}_{m,n}^{(j)}\equiv\left[\gamma_{m,n}-C^{(j)}\boldsymbol{\Delta}_m\right]\boldsymbol{\Delta}_m\hat{w}_{m,n}^{(j)}=0,\tag{11}$$

where

$$\boldsymbol{\Delta}_m\equiv\boldsymbol{\Delta}_m^{\mathrm{H}}+\partial_{zz}\equiv\partial_{rr}+\frac{1}{r}\partial_r-\frac{m^2}{r^2}+\partial_{zz}.\tag{12}$$

is the Laplace operator for the $m$th azimuthal component, and $\gamma_{m,n}\equiv\gamma_m+\mathrm{i}n\omega$ denotes the complex growth rate corresponding to the $n$th temporal harmonic. Applying separation of variables,

$$\hat{w}_{m,n}^{(j)}(r,z)=\Gamma_{m,n}(r)Z_{m,n}^{(j)}(z),\tag{13}$$

the radial dependence satisfies

$$\Gamma_{m,n}(r)=J_{|m|}(\beta_{m,n,i}r),\tag{14}$$

where $\beta_{m,n,i}$ is the $i$th eigenvalue determined from the no-penetration boundary condition at the cylinder wall,

$$\partial_r\hat{w}|_{r=1/\xi}=0.\tag{15}$$

The corresponding Bessel modes, $J_{|m|}(\beta_{m,n,i}r)$, are mutually orthogonal,

$$\left\langle J_{|m|}(\beta_{m,\cdot,i_1}r),J_{|m|}(\beta_{m,\cdot,i_2}r)\right\rangle_r=\int_0^{1/\xi}J_{|m|}(\beta_{m,\cdot,i_1}r),J_{|m|}(\beta_{m,\cdot,i_2}r)\,r\mathrm{d}r=\mathcal{J}_{m,\cdot,i_1}\delta_{i_1,i_2},\tag{16}$$

and satisfy the radial Helmholtz eigenproblem

$$\left(\boldsymbol{\Delta}_m^{\mathrm{H}}+\beta_{m,n,i}^2\right)J_{|m|}(\beta_{m,n,i}r)=0,\tag{17}$$

indicating that $\beta$ serves as a wavenumber-like parameter characterizing the radial length scale, and is independent of both the oscillation harmonic index, $n$, and the fluid property, $j$. In the following, the dependence of $\beta$ on $n$ is omitted for simplicity, and the notation $\beta_{m,\cdot,i}$ is adopted for consistency with the other variables.

Substituting the radial dependence into the governing equations (11), the axial mode associated with each Floquet harmonic can be written in the general form

$$Z_{m,n,i}^{(j)}(z)=\hat{\zeta}_{m,n,i}\left(a_{m,n,i}^{(j)}\mathrm{e}^{\beta_{m,\cdot,i}z}+b_{m,n,i}^{(j)}\mathrm{e}^{-\beta_{m,\cdot,i}z}+c_{m,n,i}^{(j)}\mathrm{e}^{\beta_{m,\cdot,i}q_{m,n,i}^{(j)}z}+d_{m,n,i}^{(j)}\mathrm{e}^{-\beta_{m,\cdot,i}q_{m,n,i}^{(j)}z}\right),\tag{18}$$

where $q_{m,n,i}^{(j)}\equiv\sqrt{1+\gamma_{m,n,i}/(C^{(j)}\beta_{m,\cdot,i})}$, and $\gamma_{m,n,i}$ is the total exponential growth rate associated with the triplet $(m,n,i)$. The no-slip boundary conditions at the top and bottom cylinder walls require that both the velocity and its

vertical derivative vanish, giving

$$\hat{w}^{(d)}_{m,n,i} = \partial_z \hat{w}^{(d)}_{m,n,i} = 0 \quad \text{at} \quad z = -1, \tag{19}$$

$$\hat{w}^{(l)}_{m,n,i} = \partial_z \hat{w}^{(l)}_{m,n,i} = 0 \quad \text{at} \quad z = 1. \tag{20}$$

At the interface $z = \zeta$, the continuity of velocity and tangential stress, and the kinematic boundary condition, yield

$$\left[1,\ \partial_z,\ \eta\left(\partial_{zz} + \beta^2_{m,\cdot,i}\right)\right] \hat{w}^{(l)}_{m,n,i} = \left[1,\ \partial_z,\ \left(\partial_{zz} + \beta^2_{m,\cdot,i}\right)\right] \hat{w}^{(d)}_{m,n,i}, \tag{21}$$

$$\gamma_{m,n,i}\hat{\zeta}_{m,n,i} = \hat{w}_{m,n,i}|_{z=0}. \tag{22}$$

For a given azimuthal wavenumber–mode pair $(m, i)$, substituting the general solution in equation (18) into the above boundary conditions leads to an 8-equation system,

$$\boldsymbol{Q}\left(a^{(d)}, b^{(d)}, c^{(d)}, d^{(d)}, a^{(l)}, b^{(l)}, c^{(l)}, d^{(l)}\right)^{\mathsf{T}} = \left(\gamma, 0, 0, 0, 0, 0, 0, 0\right)^{\mathsf{T}}. \tag{23}$$

Here, the dependence on $m$, $n$, and $i$ is omitted for simplicity.

To relate different Floquet harmonic orders, $\hat{\zeta}_{m,n,i}$, we revisit the pressure-jump condition in equation (9), which can be written in the modal form as

$$\left[\frac{\gamma_{m,n,i}}{\beta^2_{m,n,i}} + \frac{(1-\eta)(1+\mathrm{At})}{\mathrm{At}}\left(3 - \frac{\partial_{zz}}{\beta^2_{m,n,i}}\right)\right]\partial_z \hat{w}_{m,n,i} + \left(2g_{\mathrm{sgn}} - \frac{1+\mathrm{At}}{\mathrm{At}\,\mathrm{Bd}}\boldsymbol{\Delta}^{\mathrm{H}}_m\right)\hat{\zeta}_{m,n,i} = a\left(\hat{\zeta}_{m,n-1,i} + \hat{\zeta}_{m,n+1,i}\right). \tag{24}$$

The resulting linear system can be expressed as

$$\left[\underbrace{\begin{pmatrix} \ddots & \vdots & \vdots & \vdots & \vdots \\ \cdots & A_{m,-1,i} & 0 & 0 & \cdots \\ \cdots & 0 & A_{m,0,i} & 0 & \cdots \\ \cdots & 0 & 0 & A_{m,1,i} & \cdots \\ \vdots & \vdots & \vdots & \vdots & \ddots \end{pmatrix}}_{\boldsymbol{A}_{m,\cdot,i}} - a\underbrace{\begin{pmatrix} \ddots & \vdots & \vdots & \vdots & \vdots \\ \cdots & 0 & 1 & 0 & \cdots \\ \cdots & 1 & 0 & 1 & \cdots \\ \cdots & 0 & 1 & 0 & \cdots \\ \vdots & \vdots & \vdots & \vdots & \ddots \end{pmatrix}}_{\boldsymbol{B}}\right]\underbrace{\begin{pmatrix} \vdots \\ \hat{\zeta}_{m,-1,i} \\ \hat{\zeta}_{m,0,i} \\ \hat{\zeta}_{m,1,i} \\ \vdots \end{pmatrix}}_{\hat{\boldsymbol{\zeta}}_{m,\cdot,i}} = 0, \quad \text{where} \tag{25}$$

$$A_{m,n,i}(\gamma_{m,n,i};\beta_{m,\cdot,i}) \equiv \tag{26}$$

$$\beta_{m,\cdot,i}\left(a_{m,n,i} - b_{m,n,i} + c_{m,n,i}q^{(d)}_{m,n,i} - d_{m,n,i}q^{(d)}_{m,n,i}\right)\left(2\gamma_{m,n,i}/(C\beta^2_{m,\cdot,i}) + 3C(1-\eta)(1+\mathrm{At})/(\mathrm{At})\right)$$

$$- C(1-\eta)\beta_{m,\cdot,i}(1+\mathrm{At})/(\mathrm{At})\left(a_{m,n,i} - b_{m,n,i} + c_{m,n,i}q^{(d)^3}_{m,n,i} - d_{m,n,i}q^{(d)^3}_{m,n,i}\right) + (2g_{\mathrm{sgn}} + \beta^2_{m,\cdot,i}(1+\mathrm{At})/(\mathrm{At}\,\mathrm{Bd})).$$

Equations (25) and (26) provide a comprehensive analysis of interfacial instabilities, accounting for finite fluid-layer depth, viscosity effects, surface tension, internal density differences, and external vibrations. For each wavenumber, the solution of the optimization problem

$$\gamma^{(U)}_{m,\cdot,i} = \underset{\det\{\boldsymbol{A}_{m,\cdot,i}(\gamma_{m,\cdot,i};\beta_{m,\cdot,i}) - a\boldsymbol{B}\}=0}{\operatorname{argmax}} \mathrm{Re}\{\gamma_{m,\cdot,i}\}. \tag{27}$$

yields the corresponding most unstable Floquet exponent. The periodic components at different harmonics, $\hat{\boldsymbol{\zeta}}_{m,\cdot,i}$, can be then found as the null space of $(\boldsymbol{A}_{m,\cdot,i} - a\boldsymbol{B})$. Equation (27) provides a generalized analysis of the hydrodynamic instability in fluid mixing, covering a range of configuration parameters, including viscosity, surface tension, vibration,

and density differences, and exhibiting rich mechanical behavior. In the static limit ($a \to 0$), equation (27) reduces to

$$\gamma^{(U)}_{m,0,i} = \mathrm{Re}\{\gamma_{m,0,i}\} \quad \text{subject to} \quad A_{m,0,i}(\gamma_{m,0,i};\, \beta_{m,\cdot,i}) = 0, \tag{28}$$

which recovers the well-known RT dispersion relation [22]. The critical acceleration, $a_c$, for neutral stability is obtained by constraining the displacement in equation (27) to exhibit pure sinusoidal harmonic (H), $\gamma^{(U)} = 0$, or subharmonic (S), $\gamma^{(U)} = \mathrm{i}\omega/2$, responses, which recovers the generalized eigenvalue problem,

$$\boldsymbol{A}_{m,\cdot,i}\left(\gamma^{(U)}_{m,\cdot,i} = 0 \text{ or } \mathrm{i}\omega/2;\, \beta_{m,\cdot,i}\right)\hat{\boldsymbol{\xi}}_{m,\cdot,i} = a_c \boldsymbol{B}\hat{\boldsymbol{\xi}}_{m,\cdot,i}, \tag{29}$$

for the Faraday instability [20, 21]. Equation (10) also enables the prediction of transient wave dynamics for the azimuthal wavenumber–mode pair $(m, i)$ within the unstable regime. Together, these analyses enable the dissection of the mechanics as the system transitions toward nonlinear interface breakup. While standard Floquet exponents, often obtained through the eigendecomposition of the monodromy matrix, are not unique, they collectively describe nonmodal growth. Using numerical simulations, we demonstrate that the modal growth of the most unstable Floquet exponent, $\gamma^{(U)}_{m,\cdot,i}$, combined with the periodic components, can accurately predict the initial transient dynamics.

### C. Flow field dynamics

For each azimuthal wavenumber $m$, linear Floquet stability analysis yields a discrete set of radial modes, $\Gamma_{m,\cdot,i}(r) = J_m(\beta_{m,\cdot,i}r)$, the associated vertical structures, $Z_{m,n,i}(z)$, and the temporal dependence of each Floquet harmonic,

$$a_{m,n,i}(t) = \hat{\xi}_{m,n,i}\mathrm{e}^{\mathrm{i}n\omega(t+t_0)+\gamma_m t}. \tag{30}$$

To enforce incompressibility, we express the perturbation velocity field in poloidal–toroidal form,

$$\boldsymbol{u}_m(r,z,t) = \boldsymbol{\nabla}\times\boldsymbol{\nabla}\times\left(a(t)\Gamma_m(r)Z(z)\mathrm{e}^{\mathrm{i}m\theta}\boldsymbol{e}_z\right) = \mathrm{e}^{\mathrm{i}m\theta}\sum_i\sum_{n=-\infty}^{\infty} a_{m,n,i}(t)\boldsymbol{\Phi}_{m,n,i}(r,z), \tag{31}$$

with spatial basis functions for the cylindrical velocity components given by

$$\boldsymbol{\Phi}_{m,n,i}(r,z) \equiv \begin{bmatrix} \frac{1}{\beta_{m,\cdot,i}}J'_m(\beta_{m,\cdot,i}r)\, Z'_{m,n,i}(z) \\ \frac{\mathrm{i}m}{\beta^2_{m,\cdot,i}r}J_m(\beta_{m,\cdot,i}r)\, Z'_{m,n,i}(z) \\ J_m(\beta_{m,\cdot,i}r)\, Z_{m,n,i}(z) \end{bmatrix}. \tag{32}$$

Since the radial eigenfunctions are independent of the Floquet harmonic $n$, the velocity components may be rearranged to separate the radial dependence from the $(z,t)$-dependence as

$$\begin{bmatrix} u_r \\ u_\theta \\ w \end{bmatrix}_m = \mathrm{e}^{\mathrm{i}m\theta}\sum_i \begin{bmatrix} \frac{1}{\beta_{m,\cdot,i}}J'_m(\beta_{m,\cdot,i}r) \\ \frac{\mathrm{i}m}{\beta^2_{m,\cdot,i}r}J_m(\beta_{m,\cdot,i}r) \\ J_m(\beta_{m,\cdot,i}r) \end{bmatrix} \circ \left( \sum_{n=-\infty}^{\infty} a_{m,n,i}(t) \begin{bmatrix} Z'_{m,n,i} \\ Z'_{m,n,i} \\ Z_{m,n,i} \end{bmatrix}(z) \right), \tag{33}$$

where $\circ$ denotes the Hadamard product. While the radial eigenfunctions are identical for the two fluids, the axial structure in the linear regime is separated across the unperturbed interface as

$$[Z,\, Z']_{m,n,i}(z) = \begin{cases} [Z,\, Z']^{(d)}_{m,n,i}(z), & \text{if } z \le 0 \\ [Z,\, Z']^{(l)}_{m,n,i}(z), & \text{if } z > 0. \end{cases} \tag{34}$$

Equation (33) provides a compact linear spatiotemporal description of the 3D perturbation field in terms of Floquet harmonics $n$, azimuthal wavenumber $m$, and radial eigenfamilies indexed by $i$. It therefore enables the prediction of linear-regime dynamics across parametric variations in density contrast and vibration amplitude and frequency.

## IV. Numerical method

To validate the linear theory predictions and further investigate the subsequent nonlinear dynamics, high-fidelity 3D direct numerical simulations (DNS) will be conducted using MFC, a GPU-accelerated compressible solver for multi-component, multiphase flows [23]. MFC is selected for its computational efficiency, state-of-the-art GPU and superchip acceleration [24–26], and its ability to handle numerically challenging problems, such as multi-component high-density ratio flows.

The five-equation diffuse-interface model [27] is used to describe the multiphase system. The governing equations have the form

$$\frac{\partial \boldsymbol{q}}{\partial t} + \boldsymbol{\nabla} \cdot \boldsymbol{F}(\boldsymbol{q}) + \boldsymbol{h}(\boldsymbol{q}) \boldsymbol{\nabla} \cdot \boldsymbol{u} = \boldsymbol{s}(\boldsymbol{q}), \tag{35}$$

for which

$$\boldsymbol{q} = \begin{bmatrix} \alpha^{(1)} \\ \alpha^{(1)}\rho^{(1)} \\ \alpha^{(2)}\rho^{(2)} \\ \rho \boldsymbol{u} \\ \rho E \end{bmatrix}, \boldsymbol{F} = \begin{bmatrix} \alpha^{(1)}\boldsymbol{u} \\ \alpha^{(1)}\rho^{(1)}\boldsymbol{u} \\ \alpha^{(2)}\rho^{(2)}\boldsymbol{u} \\ \rho \boldsymbol{u}\boldsymbol{u} + p\boldsymbol{I} - \boldsymbol{T} \\ (\rho E + p)\boldsymbol{u} - \boldsymbol{T} \cdot \boldsymbol{u} \end{bmatrix}, \boldsymbol{h} = \begin{bmatrix} -\alpha^{(1)} \\ 0 \\ 0 \\ \boldsymbol{0} \\ 0 \end{bmatrix}, \boldsymbol{s} = \begin{bmatrix} 0 \\ 0 \\ 0 \\ -\rho \tilde{\boldsymbol{g}} \\ -\rho(\boldsymbol{u} \cdot \tilde{\boldsymbol{g}}) \end{bmatrix}. \tag{36}$$

For each fluid $j$, $\alpha^{(j)}$ is the volume fraction, $e^{(j)}$ is the internal energy, and

$$\boldsymbol{T}^{(j)} \equiv \mu^{(j)} \left[ \boldsymbol{\nabla u} + (\boldsymbol{\nabla u})^{\mathsf{T}} - \frac{2}{3} (\boldsymbol{\nabla} \cdot \boldsymbol{u}) \boldsymbol{I} \right] \tag{37}$$

is the viscous stress tensor. The equations are closed by the usual set of mixture rules

$$\sum_j \alpha^{(j)} = 1, \quad \rho = \sum_j \rho^{(j)} \alpha^{(j)}, \quad \mu = \sum_j \mu^{(j)} \alpha^{(j)}, \quad \boldsymbol{u} = \sum_j \boldsymbol{u}^{(j)} \alpha^{(j)}, \quad \text{and} \quad \boldsymbol{T} = \sum_j \boldsymbol{T}^{(j)} \alpha^{(j)}. \tag{38}$$

By aggregating the contributions from each phase through their respective mass fractions, $Y^{(j)} = \alpha^{(j)}\rho^{(j)}/\rho$, the total mixture energy $E$ is obtained as

$$E = \sum_j Y^{(j)} e^{(j)} + ||\boldsymbol{u}||^2/2. \tag{39}$$

The system is solved using a fifth-order accurate finite-volume method and a third-order accurate SSP–TVD Runge–Kutta temporal discretization. The numerical method closely follows that of Coralic and Colonius [28] and is described in detail in Bryngelson et al. [23] and Wilfong et al. [25]. Special treatment of the axis singularity in cylindrical coordinates is described in [29]. Closure is provided by the stiffened gas equation of state

$$e^{(j)} = \frac{p^{(j)} + \gamma^{(j)} \pi_{\infty,j}}{\left(\gamma^{(j)} - 1\right) \rho^{(j)}}. \tag{40}$$

The fluid parameters for the ratio of specific heats $\gamma^{(j)}$ and liquid stiffness $\pi_{\infty,j}$ enable faithful modeling of liquids and gases [30].

## V. Results

To demonstrate the linear theory predictions and numerical simulations, we adopt the cylindrical geometry and fluid configuration of the experiments in Shao et al. [14]. The cylindrical container has a radius of $R = 0.035\,\mathrm{m}$ and consists of two layers of fluid of equal depth $H = 0.022\,\mathrm{m}$, giving an aspect ratio of $\xi = 0.6286$. Doubly deionized water is chosen as the denser fluid and is characterized by density of $\rho^{(d)} = 997\,\mathrm{kg/m^3}$, kinematic viscosity of $\nu^{(d)} = 10^{-6}\,\mathrm{m^2/s}$, and surface tension coefficient of $\sigma^{(d)} = 7.2 \times 10^{-2}\,\mathrm{N/m}$. The gravitational acceleration is $g = 9.81\,\mathrm{m/s^2}$, which gives the dimensionless parameters $C = 9.814 \cdot 10^{-5}$, and Bd = 65.747, quantifying the ratios of viscous and capillary forces to gravitational forces, respectively. To model a free surface, the lighter phase is taken in the limiting ratios of At = 1 and $\eta = 0$, corresponding to vanishing density and viscosity relative to the water layer.

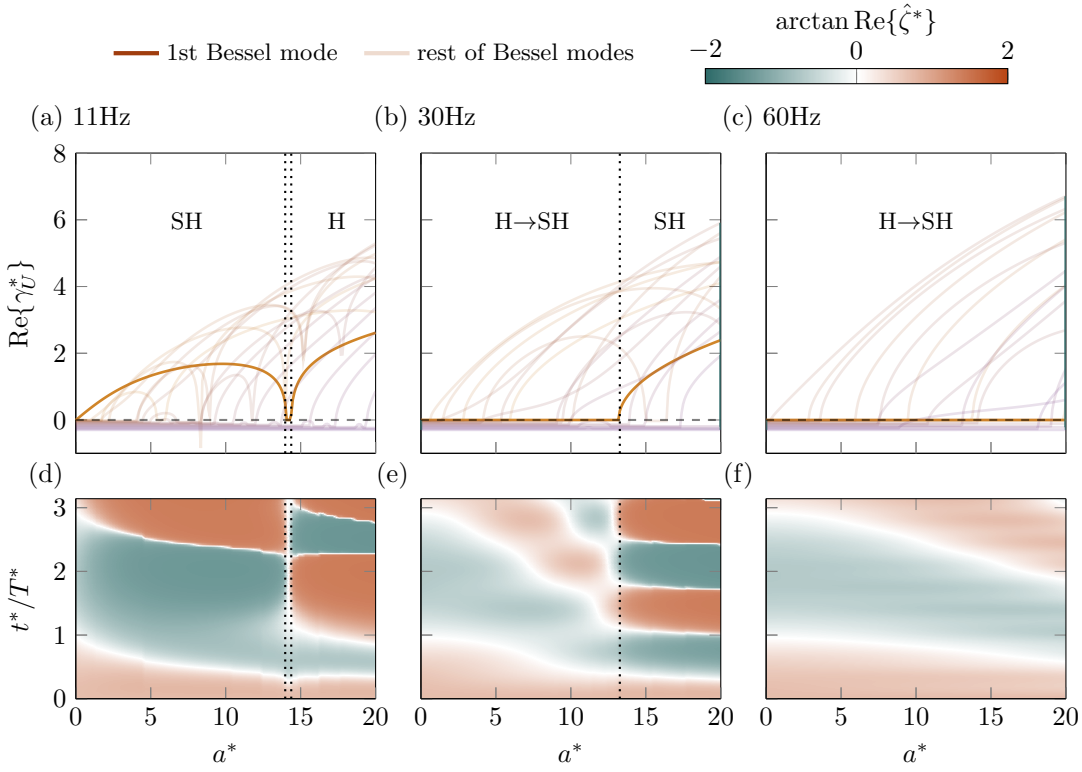


**Fig. 1 Growth rates of the axisymmetric component ($m = 0$) without the RT instability ($g_{\mathrm{sgn}} = 1$) at different oscillation frequencies: (a) 11 Hz; (b) 30 Hz; and (c) 60 Hz. The transitions between subharmonic (SH, $\mathrm{Im}(\gamma_U^*) = \mathrm{i}\omega^*/2$) and harmonic (H, $\mathrm{Im}(\gamma_U^*) = 0$) responses are highlighted. The corresponding normalized interface displacements for the first Bessel mode ($i = 1$) are shown in panels (d–f).**

We begin by considering the axisymmetric component ($m = 0$) in the absence of RT instability ($g_{\mathrm{sgn}} = 1$). Figure 1 (a-c) shows the growth rates for various Bessel modes at three different vibration frequencies. The frequency of 11 Hz, shown in panel 1(a), corresponds to the natural frequency of the first Bessel mode for the Faraday instability [14]. Consistent with this resonance condition, the linear theory predicts a positive growth rate for small, but non-zero, forcing amplitudes. As the oscillation amplitude increases, higher-order Bessel modes also become unstable and begin to dominate the system's dynamics. Concurrently, the first Bessel mode undergoes a transition in its temporal response, shifting from subharmonic (SH) to harmonic (H) behavior. This transition is also reflected in the normalized growth of the first Bessel mode relative to the initial disturbance, as shown in fig. 1(d–e). At higher oscillation frequencies, higher-order Bessel modes become unstable first as the oscillation amplitude increases. The first Bessel mode remains stable with harmonic oscillations until a critical bifurcation threshold is reached, beyond which it begins to exhibit subharmonic growth.

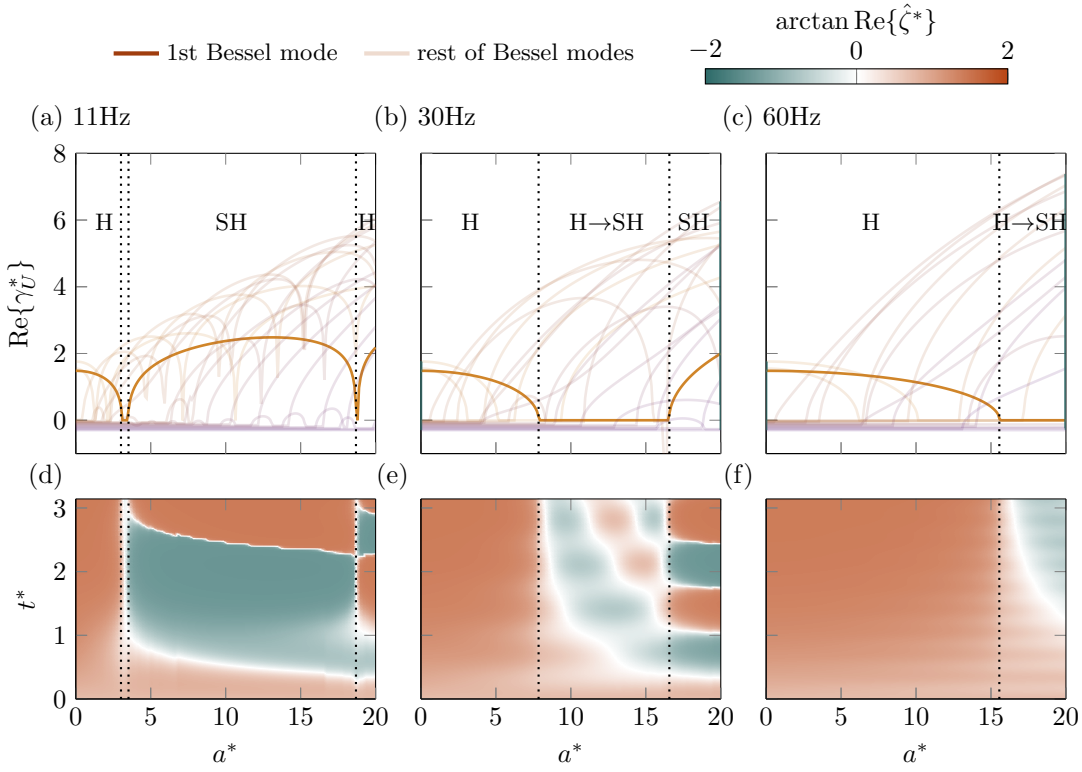


**Fig. 2 Growth rates of the axisymmetric component ($m = 0$) with static RT instability ($g_{\text{sgn}} = -1$) at different oscillation frequencies: (a) 11 Hz; (b) 30 Hz; and (c) 60 Hz. The transitions between subharmonic (SH, $\text{Im}(\gamma_U^*) = \text{i}\omega^*/2$) and harmonic (H, $\text{Im}(\gamma_U^*) = 0$) responses are highlighted. The corresponding normalized interface displacements for the first Bessel mode ($i = 1$) are shown in panels (d–f).**

Next, we consider the case in which RT and Faraday instabilities coexist, specifically under an inverted gravitational configuration where gravity acts from the denser fluid toward the lighter one ($g_{\text{sgn}} = -1$). In the limit of small oscillation amplitude ($a \to 0$), the first few Bessel modes with small wavenumber-like parameters, $\beta$, are unstable, reminiscent of the classical RT instability at small wavenumbers. As the oscillation amplitude increases, the initially unstable RT modes are progressively stabilized. Beyond a critical amplitude, the system undergoes a transition to a subharmonic Faraday response. With further increase in amplitude, this subharmonic Faraday behavior then transitions to a harmonic Faraday regime. A higher oscillation amplitude is required to stabilize RT waves at high oscillation frequencies. Correspondingly, the parameter region in which RT instability is suppressed without the excitation of additional Faraday modes expands as the oscillation frequency increases. These observations are consistent with earlier experimental findings [6, 7] and theoretical analyses of dynamic stabilization [8, 31–34] in cylindrical containers.

To have a more comprehensive understanding of the instability mechanisms, we compare the growth rates for the Faraday-only case and the mixed Faraday–RT case in fig. 3. In both cases, the growth rates of adjacent Bessel modes can differ due to the discontinuous nature of the wavenumber-like parameter, $\beta_{m,\cdot,i}$ This result indicates that each mode responds differently to the imposed vibration. At higher oscillation amplitudes, this discontinuity becomes less pronounced, as the dominance of the Faraday instability leads to more uniform responses across adjacent modes. Additionally, higher-order Faraday peaks emerge beyond the fundamental one. These mode-dependent differences are more pronounced at lower oscillation frequencies, particularly when Faraday and RT instabilities coexist. As a result, the interfacial dynamics can become complex when multiple unstable modes are simultaneously excited.

We also examine the growth rates for the dipolar component ($m = 1$). The overall trends are similar to those observed for the axisymmetric component, indicating that external vibration can excite not only radial modes but also higher-order

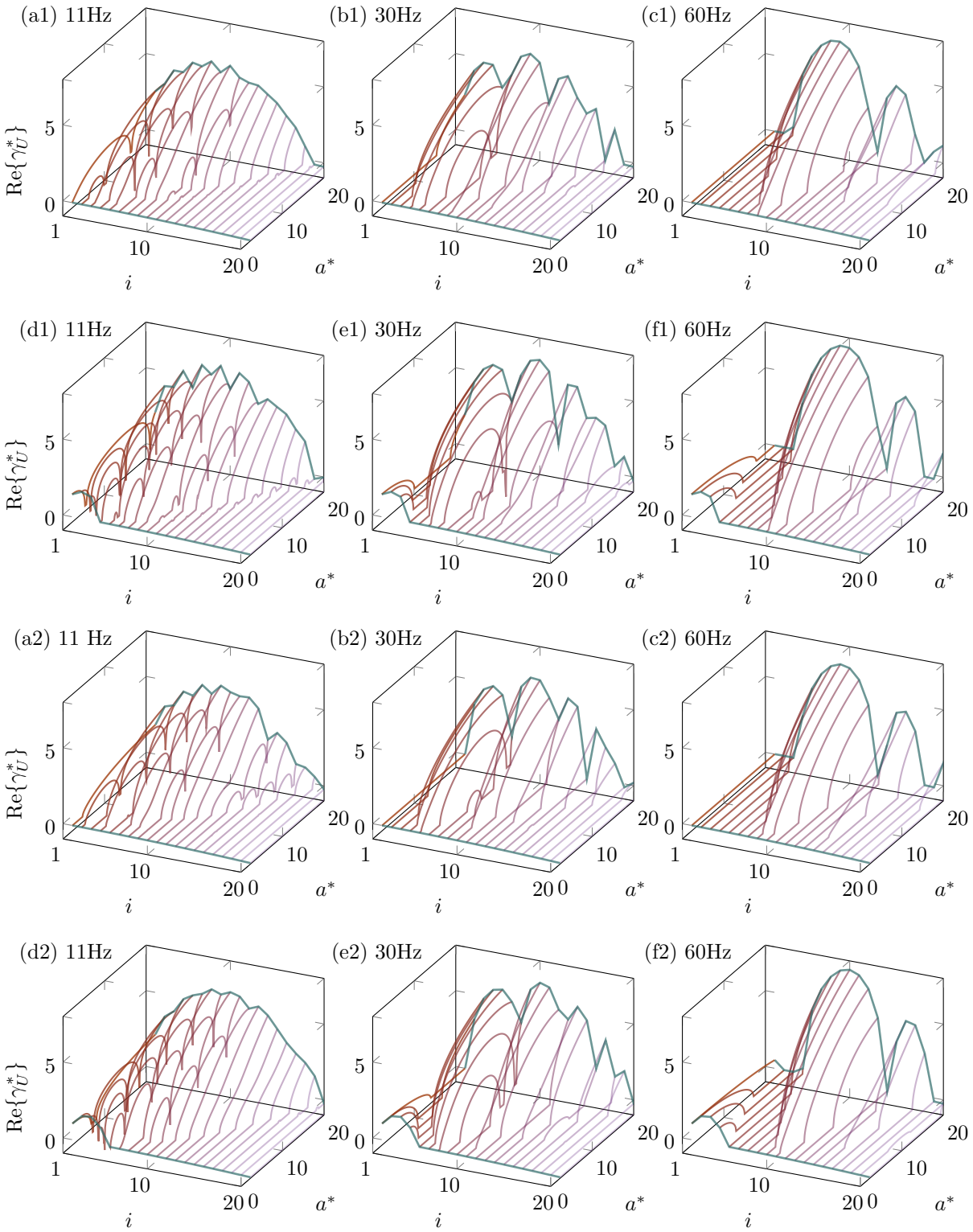


**Fig. 3 Growth rates of the axisymmetric ($m$ = 0; panels a1–f1) and dipolar ($m$ = 1; panels a2-f2) modes for the Faraday-only case (a1–c1, a2-c2) and the mixed Faraday–RT case (d1–f1, d2-f2). Three oscillation frequencies are considered: (a1,d1,a2,d2) 11 Hz; (b1,e1,b2,e2) 30 Hz; and (c1,f1,c2,f2) 60 Hz.**

azimuthal modes through the same instability mechanisms. Consequently, for initial disturbances containing appreciable energy in multiple azimuthal components, strong nonlinear mode interactions are anticipated, especially when several modes have comparable growth rates.

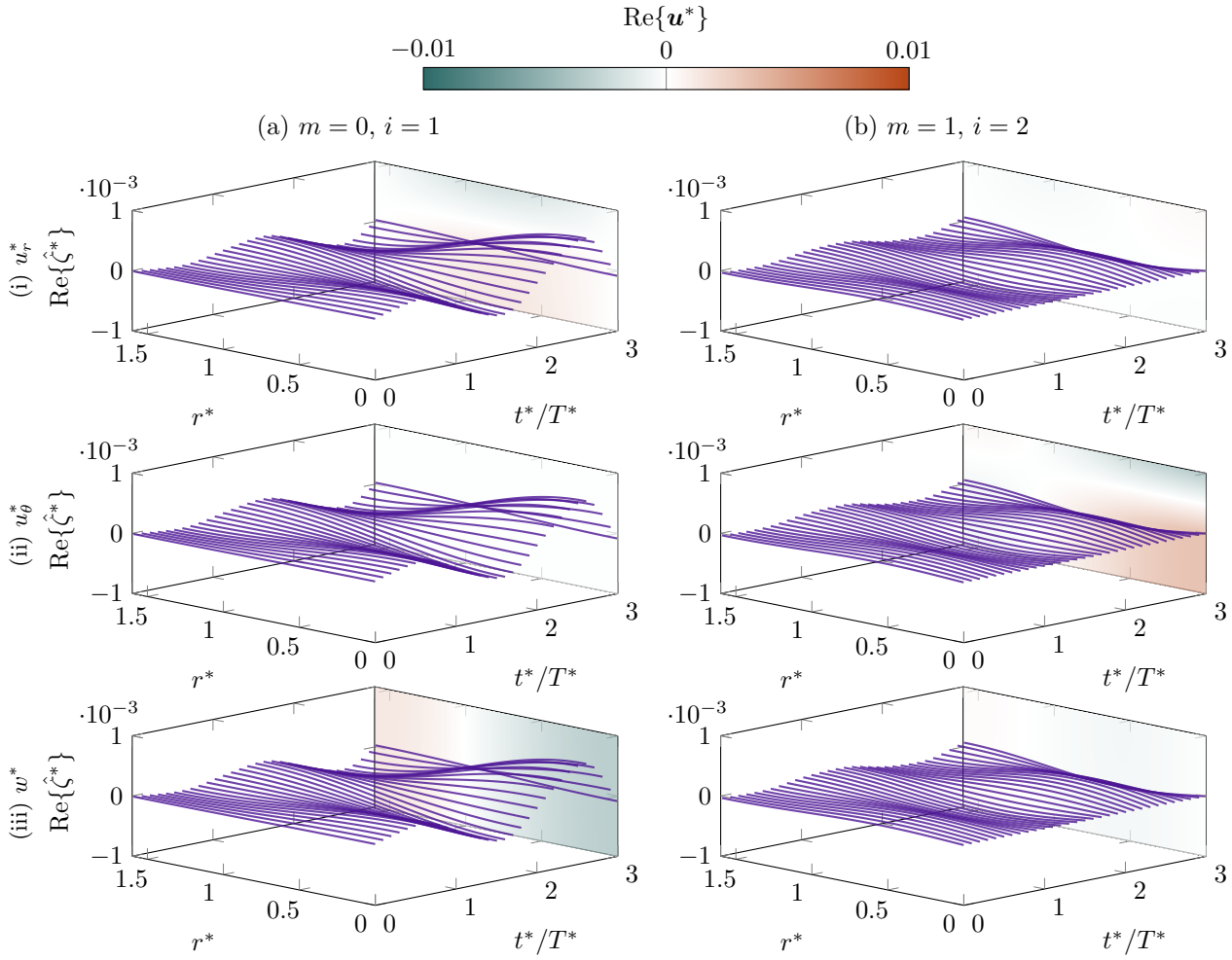


**Fig. 4 Linear-Floquet-theory predictions of the interfacial displacement and velocity fields at $t^*/T^* = 3$ for the Faraday-only configuration ($g_{\mathrm{sgn}} = 1$) at vibration amplitude $a^* = 0.9$ and frequency $\omega = 11$ Hz: (a) $m = 0, i = 1$; (b) $m = 1$, $i = 2$.**

As an example, fig. 4 shows the flow field and interfacial response in the Faraday-only configuration at forcing amplitude $a^* = 0.9$ and frequency $\omega = 11$ Hz, as predicted by Linear Floquet theory. As shown in fig. 3, both the axisymmetric and dipolar components are unstable under these conditions. Although their growth rates have comparable real parts, the resulting interfacial dynamics differ markedly: the axisymmetric mode exhibits substantially larger-amplitude oscillations than the dipolar mode. Importantly, the displacement at the axis cannot be represented by any non-axisymmetric azimuthal component and can only be balanced by the $m = 0$ contribution, potentially involving additional radial Bessel modes. The dipolar response is accompanied by a non-zero azimuthal-velocity component, whereas the axisymmetric mode has $u_\theta = 0$ by the boundary conditions.

Figure 5 visualizes the 3D simulation results for the Faraday-only configuration ($g_{\mathrm{sgn}} = 1$) at vibration amplitude $a^* = 10$ and frequency $\omega = 11$ Hz, without surface tension. The initial interface is perturbed by the first radial mode of the axisymmetric component ($m = 0, i = 1$), with an amplitude of 0.005. As shown in fig. 1(a), the linear Floquet stability analysis predicts an unstable subharmonic Faraday response for this configuration. This subharmonic nature

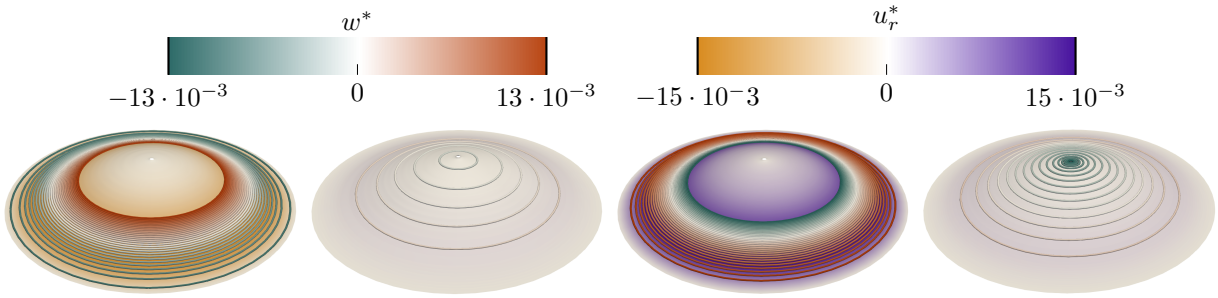


**(a)** $t^*/T^* = 0.25$ **(b)** $t^*/T^* = 0.50$ **(c)** $t^*/T^* = 0.75$ **(d)** $t^*/T^* = 1.00$

**Fig. 5 Three-dimensional simulation for the Faraday-only configuration ($g_{\text{sgn}} = 1$) at vibration amplitude $a^* = 10$ and frequency $\omega = 11$ Hz, without surface tension. The initial interface is perturbed by the first radial mode of the axisymmetric component ($m = 0, i = 1$) with amplitude of $0.005$. The instantaneous interface is colored by the radial velocity $u_r^*$ and overlaid with equally spaced contours of the vertical velocity $w^*$.**

is confirmed by the reversal in the sign of the simulated velocity field between $t^*/T^* = 0.25$ and $t^*/T^* = 0.75$. By resolving the full spatiotemporal evolution of the flow field, the 3D DNS provides a direct means to examine how vibration and density contrast jointly govern the interfacial dynamics in confined cylindrical systems.

## VI. Summary

This study combines linear Floquet stability analysis with three-dimensional direct numerical simulations (DNS) to investigate interfacial instabilities in vertically vibrated cylindrical containers. In the presence of both an external forcing and an internal density contrast, two fundamental hydrodynamic instabilities arise: the pressure-gradient-driven Rayleigh–Taylor (RT) instability and the parametric, resonance-induced Faraday instability. We characterize the onset and dynamics of the instabilities across the oscillation frequency–amplitude parameter space, resolved by azimuthal wavenumber, Floquet harmonic, and radial (Bessel) mode index.

In cylindrical geometry, the dominant spatial structures are naturally organized into Bessel eigenmodes for each azimuthal wavenumber: RT dynamics are dominated by long-wavelength modes that grow steadily, whereas Faraday responses excite shorter-wavelength modes exhibiting harmonic or subharmonic Floquet time dependence. The corresponding growth rates are predicted by linear Floquet analysis and verified by simulations for the RT-stable configuration (gravity directed from the lighter fluid toward the denser). In the RT-unstable case, increasing the vibration amplitude reveals a three-regime sequence: a low-amplitude, steadily growing RT-dominated response; a transition beyond a critical amplitude to a subharmonic Faraday regime; and, under stronger forcing, a further transition to a harmonic Faraday regime. Beyond the interfacial response, we analyze the full spatiotemporal evolution of the flow field using linear theory and simulation, showing how vibration and density contrast jointly affect the flow dynamics in confined cylindrical systems.

## Acknowledgments

This work used the resources of the Oak Ridge Leadership Computing Facility at the Oak Ridge National Laboratory, which is supported by the Office of Science of the U.S. Department of Energy under Contract No. DE-AC05-00OR22725 (PIs Bryngelson and McMullen, allocations CFD154 and ENG160). This work also used NCSA Delta at the NCSA and Bridges2 at the Pittsburgh Supercomputing Center through allocation TG-PHY210084 (PI Spencer Bryngelson) from the Advanced Cyberinfrastructure Coordination Ecosystem: Services & Support (ACCESS) program, which is supported by National Science Foundation grants #2138259, #2138286, #2138307, #2137603, and #2138296.

Sandia National Laboratories is a multi-mission laboratory managed and operated by National Technology & Engineering Solutions of Sandia, LLC (NTESS), a wholly owned subsidiary of Honeywell International Inc., for the U.S. Department

of Energy's National Nuclear Security Administration (DOE/NNSA) under contract DE-NA0003525. 

## References

[1] Craxton, R. S., Anderson, K. S., Boehly, T. R., Goncharov, V. N., Harding, D. R., Knauer, J. P., McCrory, R. L., McKenty, P. W., Meyerhofer, D. D., Myatt, J. F., et al., "Direct-drive inertial confinement fusion: A review," *Phys. Plasmas*, Vol. 22, No. 11, 2015.

[2] Betti, R., and Hurricane, O. A., "Inertial-confinement fusion with lasers," *Nat. Phys.*, Vol. 12, No. 5, 2016, pp. 435–448.

[3] L., R., "Investigation of the character of the equilibrium of an incompressible heavy fluid of variable density," *Proc. London Math. Soc.*, Vol. 1, No. 1, 1882, pp. 170–177.

[4] Taylor, G. I., "The instability of liquid surfaces when accelerated in a direction perpendicular to their planes. I," *Phil. Trans. R. Soc. A*, Vol. 201, No. 1065, 1950, pp. 192–196.

[5] Faraday, M., "XVII. On a peculiar class of acoustical figures; and on certain forms assumed by groups of particles upon vibrating elastic surfaces," *Phil. Trans. R. Soc.*, , No. 121, 1831, pp. 299–340.

[6] Wolf, G. H., "The dynamic stabilization of the Rayleigh–Taylor instability and the corresponding dynamic equilibrium," *Z. Physik*, Vol. 227, No. 3, 1969, pp. 291–300.

[7] Wolf, G. H., "Dynamic stabilization of the interchange instability of a liquid-gas interface," *Phys. Rev. Lett.*, Vol. 24, No. 9, 1970, p. 444.

[8] Lapuerta, V., Mancebo, F. J., and Vega, J. M., "Control of Rayleigh–Taylor instability by vertical vibration in large aspect ratio containers," *Phys. Rev. E*, Vol. 64, No. 1, 2001, p. 016318.

[9] Haimovich, O., and Oron, A., "Nonlinear dynamics of a thin liquid film on an axially oscillating cylindrical surface," *Phys. Fluids*, Vol. 22, No. 3, 2010.

[10] Liang, Y., and Luo, X., "Experimental investigation of cylindrically divergent Rayleigh–Taylor instability on a water–air interface," *J Fluid Mech.*, Vol. 1016, 2025, p. R2.

[11] Miles, J. W., "Nonlinear faraday resonance," *J. Fluid Mech.*, Vol. 146, 1984, pp. 285–302.

[12] Miles, J., and Henderson, D., "Parametrically forced surface waves," *Annu. Rev. Fluid Mech.*, Vol. 22, No. 1, 1990, pp. 143–165.

[13] Henderson, D., and Miles, J., "Surface-wave damping in a circular cylinder with a fixed contact line," *J. Fluid Mech.*, Vol. 275, 1994, pp. 285–299.

[14] Shao, X., Wilson, P., Saylor, J., and Bostwick, J., "Surface wave pattern formation in a cylindrical container," *J. Fluid Mech.*, Vol. 915, 2021, p. A19.

[15] Zhang, S., Borthwick, A. G., and Lin, Z., "Pattern evolution and modal decomposition of Faraday waves in a brimful cylinder," *J. Fluid Mech.*, Vol. 974, 2023, p. A56.

[16] Batson, W., Zoueshtiagh, F., and Narayanan, R., "The Faraday threshold in small cylinders and the sidewall non-ideality," *J. Fluid Mech.*, Vol. 729, 2013, pp. 496–523.

[17] Dinesh, B., Livesay, J., Ignatius, I., and Narayanan, R., "Pattern formation in Faraday instability—experimental validation of theoretical models," *Philos. Trans. R. Soc. A*, Vol. 381, No. 2245, 2023, p. 20220081.

[18] Chu, T., Wilfong, B., Koehler, T., McMullen, R. M., and Bryngelson, S. H., "Competing mechanisms at vibrated interfaces of density-contrast fluids," *Phys. Rev. Fluids*, Vol. 10, No. 9, 2025, p. 093904.

[19] Floquet, G., "Sur les équations différentielles linéaires à coefficients périodiques," *Ann. Sci. Ecole. Norm. S.*, Vol. 12, 1883, pp. 47–88.

[20] Kumar, K., and Tuckerman, L. S., "Parametric instability of the interface between two fluids," *J. Fluid Mech.*, Vol. 279, 1994, pp. 49–68.

[21] Kumar, K., "Linear theory of Faraday instability in viscous liquids," *Proc. R. Soc. Lond. A*, Vol. 452, No. 1948, 1996, pp. 1113–1126.

[22] Chandrasekhar, S., *Hydrodynamic and Hydromagnetic Stability*, Oxford University Press, 1961.

[23] Bryngelson, S. H., Schmidmayer, K., Coralic, V., Meng, J. C., Maeda, K., and Colonius, T., "MFC: An open-source high-order multi-component, multi-phase, and multi-scale compressible flow solver," *Comp. Phys. Comm.*, Vol. 266, 2021, p. 107396.

[24] Radhakrishnan, A., Le Berre, H., Wilfong, B., Spratt, J.-S., Rodriguez Jr., M., Colonius, T., and Bryngelson, S. H., "Method for portable, scalable, and performant GPU-accelerated simulation of multiphase compressible flow," *Comput. Phys. Commun.*, Vol. 302, 2024, p. 109238.

[25] Wilfong, B., Le Berre, H. A., Radhakrishnan, A., Gupta, A., Vickers, D. J., Vaca-Revelo, D., Adam, D., Yu, H., Lee, H., Chreim, J. R., et al., "MFC 5.0: An exascale many-physics flow solver," *Comput. Phys. Commun.*, 2026, p. 110055.

[26] Wilfong, B., Radhakrishnan, A., Le Berre, H., Vickers, D., Prathi, T., Tselepidis, N., Dorschner, B., Budiardja, R., Cornille, B., Abbott, S., et al., "Simulating many-engine spacecraft: Exceeding 1 quadrillion degrees of freedom via information geometric regularization," *SC25*, 2025, pp. 14–24.

[27] Allaire, G., Clerc, S., and Kokh, S., "A five-equation model for the simulation of interfaces between compressible fluids," *Journal of Computational Physics*, Vol. 181, No. 2, 2002, pp. 577–616.

[28] Coralic, V., and Colonius, T., "Finite-volume WENO scheme for viscous compressible multicomponent flows," *J. Comput. Phys.*, Vol. 274, 2014, pp. 95–121.

[29] Mohseni, K., and Colonius, T., "Numerical Treatment of Polar Coordinate Singularities," *J. Comput. Phy.*, Vol. 157, No. 2, 2000, pp. 787–795.

[30] Menikoff, R., and Plohr, B. J., "The Riemann problem for fluid flow of real materials," *Rev. Mod. Phys.*, Vol. 61, 1989, pp. 75–130.

[31] Troyon, F., and Gruber, R., "Theory of the dynamic stabilization of the Rayleigh–Taylor instability," *Phys. Fluids*, Vol. 14, No. 10, 1971, pp. 2069–2073.

[32] Piriz, A. R., Rodriguez P., G., Munoz D., I., Lopez C., J. J., and Tahir, N. A., "Dynamic stabilization of Rayleigh–Taylor instability in Newtonian fluids," *Phys. Rev. E*, Vol. 82, No. 2, 2010, p. 026317.

[33] Sterman-Cohen, E., Bestehorn, M., and Oron, A., "Rayleigh–Taylor instability in thin liquid films subjected to harmonic vibration," *Phys. Fluids*, Vol. 29, No. 5, 2017.

[34] Pototsky, A., and Bestehorn, M., "Faraday instability of a two-layer liquid film with a free upper surface," *Phys. Rev. Fluids*, Vol. 1, No. 2, 2016, p. 023901.